Soft Matter

PAPER

Cite this: DOI: 10.1039/xxxxxxxxxx

Characterization of surface–solute interactions by diffusioosmosis

Jesse T. Ault,[*a] Sangwoo Shin,[b] and Howard A. Stone[c]

Received Date
Accepted Date

DOI: 10.1039/xxxxxxxxxx

www.rsc.org/journalname

The accurate measurement of wall zeta potentials and solute–surface interaction length scales for electrolyte and non-electrolyte solutes, respectively, is critical to the design of many biomedical and microfluidic applications. We present a novel microfluidic approach using diffusioosmosis for measuring either the zeta potentials or the characteristic interaction length scales for surfaces exposed to, respectively, electrolyte or non-electrolyte solutes. When flows containing different solute concentrations merge in a junction, local solute concentration gradients can drive diffusioosmotic flow due to electrokinetic, steric, and other interactions between the solute molecules and solid surfaces. We demonstrate a microfluidic system consisting of a long, narrow pore connecting two large side channels in which solute concentration gradients drive diffusioosmosis within the pore, resulting in predictable fluid velocity/pressure and solute profiles. Furthermore, we present analytical results and a methodology to determine the zeta potential or interaction length scale for the pore surfaces based on the solute concentrations in the main side channels, the flow rate in the pore, and the pressure drop across the pore. We apply this method to the experimental data of Lee *et al.*[1] to predict the zeta potentials of their system, and we use 3D numerical simulations to validate the theory and show that end effects caused by the junctions are negligible for a wide range of parameters. Because the dynamics in the proposed system are driven by diffusioosmosis, this technique does not suffer from certain disadvantages associated with the use of sensitive electronics in traditional zeta potential measurement approaches such as streaming potential, streaming current, or electroosmosis. To the best of our knowledge this is the first flow-based approach to characterize surface/solute interactions with non-electrolyte solutes.

Introduction

The zeta potential ζ is the electrical potential at the shear plane of the electric double layer, which represents a key property in a number of electrokinetics applications such as microfluidic fluid handling and manipulation, biomolecule separation, colloid stability, etc.[2,3] Two topics of recent interest in the family of electrokinetic phenomena are diffusiophoresis and diffusioosmosis, which refer, respectively, to the motion of particles and fluids driven by chemical gradients. As with electrophoresis and electroosmosis, the zeta potential dictates the magnitude of the flow of an electrolytic solution within the Debye layer in the presence of an external field gradient. For the case of diffusiophoresis and diffusioosmosis, the source of these motions are chemical solute gradients.[4,5] Recent reports suggest that diffusiophoresis and diffusioosmosis can be useful tools for a variety of applications including biomolecule separation[6–8], water purification[9–11], particle delivery in confined spaces[12–14], surface coating[15–17], zeta potentiometry[18], fabric cleaning[19], and many others.

While the majority of studies and applications of diffusiophoresis and diffusioosmosis typically involve the use of electrolyte solutes, non-electrolyte solute gradients can also drive these effects. Whereas surface/solute interactions with electrolyte solutes are usually characterized by the zeta potential, surface/solute inter-

---

[a] *Computational Sciences and Engineering Division, Oak Ridge National Laboratory, Oak Ridge, TN 37831, USA*
[b] *Department of Mechanical Engineering, University of Hawaii at Manoa, Honolulu, HI 96822, USA*
[c] *Department of Mechanical and Aerospace Engineering, Princeton University, Princeton, NJ 08544, USA*
Please address correspondance to aultjt@ornl.gov.

This manuscript has been authored by UT-Battelle, LLC under Contract No. DE-AC05-00OR22725 with the U.S. Department of Energy. The United States Government retains and the publisher, by accepting the article for publication, acknowledges that the United States Government retains a non-exclusive, paid-up, irrevocable, world-wide license to publish or reproduce the published form of this manuscript, or allow others to do so, for United States Government purposes. The Department of Energy will provide public access to these results of federally sponsored research in accordance with the DOE Public Access Plan (http://energy.gov/downloads/doe-public-access-plan). Research sponsored by the Laboratory Directed Research and Development Program of Oak Ridge National Laboratory, managed by UT-Battelle, LLC, for the U. S. Department of Energy.

actions with non-electrolyte solutes are typically characterized by the characteristic length scale of the solute–surface interaction and the Gibbs adsorption length, which is proportional to the excess amount of solute per unit area that accumulates near the surface due to the interaction potential ϕ.[20–22] The adsorption length is a measure of the strength of the adsorption, and it is positive for the case of adsorption and negative for repulsion.[22]

Since the functionality and efficacy of many applications rely on the accurate knowledge of particle/surface zeta potentials or interaction length scales (depending on the nature of the solute), accurate techniques for measuring these properties are critical for the design of such applications. For the case of electrolyte solutes, the zeta potential of colloidal particles can be measured via the commercially available electrophoretic light scattering technique or via a recent diffusiophoretic microfluidic technique[18], whereas measuring the zeta potential of solid surfaces typically relies on a number of sophisticated in-house methods including the electroosmosis, streaming potential, streaming current, and ZetaSpin methods.[23–26] These methods have demonstrated simplicity and reliability, but their reliance on precise electrical measurements and the need for high-end ammeters/voltmeters have decreased their accessibility and introduced several potential limitations that will be discussed below.[2] Furthermore, for the case of non-electrolyte solutes, none of these techniques can be adapted to measure the characteristic length scales of solute–surface interactions, since those methods all rely on the charge of the solute ions. A detailed review of these four common measurement techniques and some of their potential limitations is given in Appendix A.

While all of the previously mentioned measurement techniques have been used with success, no technique is without potential limitations and challenges. Typically the use of sensitive electronics is required, special care is needed to avoid and correct for issues including electrode polarizability and surface conductivity, chemical reactions with the electrodes can become critical at certain pH values, and, finally, all of the methods are limited to the use of electrolyte solutes. None of the proposed methods can be adapted to measure the characteristic interaction length scales for non-electrolyte solutes, which could be considered the analog of the zeta potential in electrolyte solutes. In this paper, we propose a new method that does not rely on sensitive voltage/current measurements and can be used to measure both the zeta potentials of surfaces in electrolyte solutes and non-electrostatic interactions between surfaces and non-electrolyte solutes. The proposed method relies on diffusioosmotic flow in a long, narrow channel driven by electrolyte or non-electrolyte solute concentration gradients.

The physical origin of these diffusioosmotic flows was first recognized by Derjaguin and coworkers who predicted the relative speed between the fluid flow and a solid flat plate due to solute gradients, which they experimentally confirmed.[27,28] They also recognized that these flows can cause a predictable disturbance to the fluid dynamics in small capillaries.[28] Derjaguin *et al.* derived formulas to predict this "capillary-osmotic" flow, validated these results experimentally, and suggested that such methods could potentially be used to analyze the structure of adsorption layers at solid-solution interfaces.[29] Additional studies of diffusioosmotic-driven flows in capillaries have led to models for the osmotic flow in leaky porous membranes and analytical results for the reflection coefficients in such flows for the case of purely steric solute–surface interactions.[30,31] These coefficients characterize the degree to which solute molecules are rejected from a leaky membrane.

In the following sections, we propose a technique using diffusioosmosis for measuring the zeta potential of surfaces in electrolyte solutes or the solute–surface interaction length scales of surfaces in non-electrolyte solutes. We show that flow rate and pressure drop measurements in an H-shaped microfluidics system can be used to calculate the zeta potential or interaction length scales needed to characterize the surface–solution interactions. We use 3D numerical simulations to validate the theoretical results, and we apply this method to the experimental flow rate results of Lee *et al.*[1] to show a practical demonstration of this technique.

Theory

In this section, we present analytical solutions for the fluid velocity and pressure profiles inside a narrow pore of length L that connects two main flow channels containing different solute concentrations as shown in Figure 1. The equations governing the coupled fluid/solute dynamics include the Navier-Stokes and continuity equations, as well as an advection–diffusion equation for the solute dynamics. Analytical solutions can be achieved via the lubrication approximation for the case of long, narrow pores. The unique feature that differentiates such a system from a traditional pressure-driven Poiseuille flow calculation is the addition of approximate wall slip boundary conditions on the pore walls due to diffusioosmosis driven by local solute concentration gradients. These slip boundary conditions result in predictable deviations of the velocity/pressure profiles within the pore from the Poiseuille flow case with no-slip boundaries. Using the theoretical solutions for the fluid/solute dynamics that we develop in this section, we will show that the zeta potential or interaction length scales of the surface–solution interactions can be directly related to the flow rate and the pressure drop across the pore.

Governing equations and boundary conditions

The fluid and solute dynamics within the system are governed by the coupled incompressible Navier-Stokes and continuity equations, as well as an advection–diffusion equation for the solute concentration. With the fluid velocity, pressure, density, and viscosity given respectively by $\boldsymbol{u} = (u, v, w)$, p, ρ, and μ, the solute concentration given by c, and the solute diffusivity given by D_s, the dimensional forms of the governing equations (assuming constant properties) are given by

$$\rho\left(\frac{\partial \boldsymbol{u}^*}{\partial t^*} + \boldsymbol{u}^* \cdot \nabla^* \boldsymbol{u}^*\right) = -\nabla^* p^* + \mu \nabla^{*2} \boldsymbol{u}^*, \tag{1a}$$

$$\nabla^* \cdot \boldsymbol{u}^* = 0, \tag{1b}$$

$$\frac{\partial c^*}{\partial t^*} + \boldsymbol{u}^* \cdot \nabla^* c^* = D_s \nabla^{*2} c^*, \tag{1c}$$

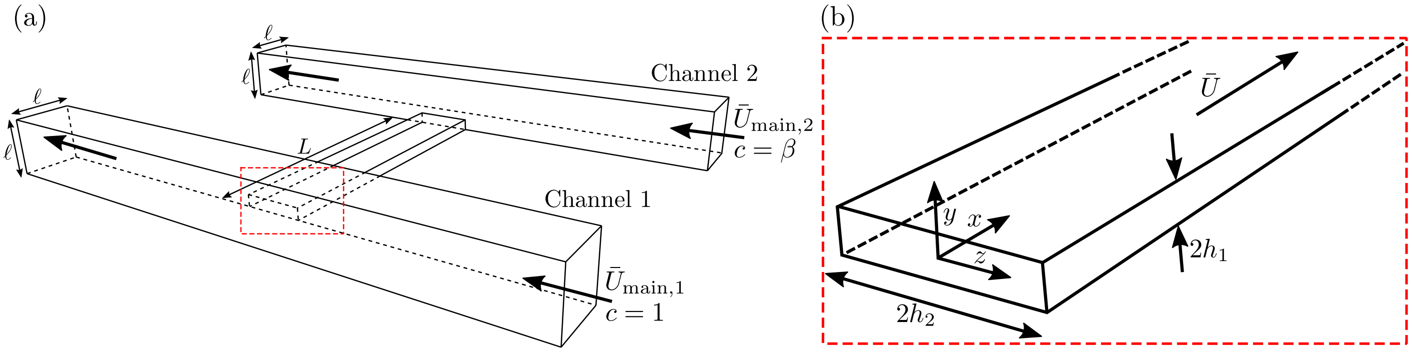

Fig. 1 Flow geometry and problem setup (not shown to scale). We consider the flow in a narrow pore of dimensions $2h_1 \times 2h_2 \times L$ that connects two larger square channels of side length ℓ. Channel 1 carries a nondimensional solute concentration of $c = 1$ at a mean speed of $\bar{U}_{\text{main},1}$, and channel 2 carries a nondimensional solute concentration of $c = \beta$ at a mean speed of $\bar{U}_{\text{main},2}$. Dynamics within the pore are established by the combined influences of fluid advection and diffusioosmosis. Slip boundary conditions at the pore walls drive recirculating secondary flows through diffusioosmosis, which cause deviations from Poiseuille flow in the pressure and velocity within the pore. The pressure drop across the pore and the mean flow velocity can be directly related to the diffusioosmotic mobility of the pore walls, making possible the use of such a system to characterize the surface–solution interactions through either the zeta potential or characteristic interaction length scales. (a) Full perspective view of the system setup. (b) Zoomed-in view of the boxed, red region denoting the entrance to the pore and the coordinate system. Solid arrows denote the direction of the flow.

where *'s denote dimensional variables. For this analysis, we will consider the steady-state form of Eqs. (1). With steady inlet/outlet conditions, the solute concentration gradient within the pore will develop over a timescale of L^2/D_s, where the flow is quasi-steady relative to the solute because we consider low-Reynolds-number flows and for typical solutes in water we have $D_s \ll \nu$. For the purposes of characterizing the surface–solution interactions, we are only interested in the steady-state fluid/solute dynamics in the pore and not the initial transient period as the solute concentration gradient develops. Steady-state is achieved when $t^* \gg L^2/D_s$, at which point the time derivatives may be safely neglected from Eqs. (1).

Beginning with the dimensional governing equations given by Eqs. (1), we nondimensionalize the axial velocity component u^* by the average axial fluid speed in the pore $\bar{U}$ and the secondary velocity components v^* and w^* by $\bar{U}h_1/L$ and $\bar{U}h_2/L$, respectively, to preserve the form of the continuity equation (see Figure 1). We further nondimensionalize x^* by the pore length L, y^* by the characteristic length in the y-direction h_1, z^* by the characteristic length in the z-direction h_2, c^* by the uniform solute concentration at the pore inlet $c^*(x = 0)$, and p by the viscous pressure scale $\mu\bar{U}L/h_1^2$. With these scalings, the governing equations can be written as

$$\mathrm{Re}\,\varepsilon_1\left(u\frac{\partial u}{\partial x} + v\frac{\partial u}{\partial y} + w\frac{\partial u}{\partial z}\right) = \varepsilon_1^2\frac{\partial^2 u}{\partial x^2} + \frac{\partial^2 u}{\partial y^2} + \frac{h_1^2}{h_2^2}\frac{\partial^2 u}{\partial z^2} - \frac{\partial p}{\partial x}, \quad \text{(2a)}$$

$$\mathrm{Re}\,\varepsilon_1\left(u\frac{\partial v}{\partial x} + v\frac{\partial v}{\partial y} + w\frac{\partial v}{\partial z}\right) = \varepsilon_1^2\frac{\partial^2 v}{\partial x^2} + \frac{\partial^2 v}{\partial y^2} + \frac{h_1^2}{h_2^2}\frac{\partial^2 v}{\partial z^2} - \frac{1}{\varepsilon_1^2}\frac{\partial p}{\partial y}, \quad \text{(2b)}$$

$$\mathrm{Re}\,\varepsilon_1\left(u\frac{\partial w}{\partial x} + v\frac{\partial w}{\partial y} + w\frac{\partial w}{\partial z}\right) = \varepsilon_1^2\frac{\partial^2 w}{\partial x^2} + \frac{\partial^2 w}{\partial y^2} + \frac{h_1^2}{h_2^2}\frac{\partial^2 w}{\partial z^2} - \frac{1}{\varepsilon_2^2}\frac{\partial p}{\partial z}, \quad \text{(2c)}$$

$$\frac{\partial u}{\partial x} + \frac{\partial v}{\partial y} + \frac{\partial w}{\partial z} = 0, \quad \text{(2d)}$$

$$\mathrm{Pe}\,\varepsilon_1^2\left(u\frac{\partial c}{\partial x} + v\frac{\partial c}{\partial y} + w\frac{\partial c}{\partial z}\right) = \varepsilon_1^2\frac{\partial^2 c}{\partial x^2} + \frac{\partial^2 c}{\partial y^2} + \frac{h_1^2}{h_2^2}\frac{\partial^2 c}{\partial z^2}, \quad \text{(2e)}$$

where $\varepsilon_i = h_i/L$, the pore Reynolds number is defined as $\mathrm{Re} = \rho\bar{U}h_1/\mu$, and the solute Peclet number is defined as $\mathrm{Pe} = L\bar{U}/D_s$. As boundary conditions, we fix the solute concentration at the inlet and outlet of the pore to be $c = 1$ at $x = 0$ and $c = \beta$ at $x = 1$, respectively (Fig. 1). Thus, we assume that the end effects where the pore merges with the main side channels are negligible and the solute concentrations at the inlet and outlet of the pore are approximately uniform and equal to the concentrations carried in the corresponding adjacent side channels. Additionally, we assume that the solute does not penetrate the walls of the pore, i.e. $\partial c/\partial y = 0$ at $y = \pm 1$ and $\partial c/\partial z = 0$ at $z = \pm 1$. The fluid flow also obeys a no-penetration condition at the pore walls, i.e. $v = 0$ at $y = \pm 1$ and $w = 0$ at $z = \pm 1$.

Finally, diffusioosmosis drives a slip velocity boundary condition at the outer edge of the double layer due to the solute concentration gradient within the pore. In the limit of infinitesimal Debye layer thickness, λ_d, relative to the channel height, this can be treated effectively as a slip velocity boundary condition at the pore walls. In the next section, we will show that the steady-state solute concentration is independent of y and z to leading order in a narrow pore, which allows the dimensionless wall slip velocity u_w to be written approximately as[21,32]

$$u_w(x) = -\frac{\Gamma_w(x)}{L\bar{U}}\frac{\mathrm{d}\ln c}{\mathrm{d}x}, \quad \text{(3)}$$

where $\Gamma_w(x)$ is the diffusioosmotic mobility of the pore surfaces, which is a function of both the solute and surface properties and will generally vary with x as the solute concentration changes. Then, in the thin Debye layer approximation, the wall slip boundary conditions are given by $u = u_w(x)$ at $y = \pm 1$ and $z = \pm 1$, $v = 0$ at $z = \pm 1$, and $w = 0$ at $y = \pm 1$. Note that the Debye layer thickness varies as $c^{*-1/2}$ and can be estimated as $\lambda_d \approx 30$ nm with $c^* = 0.1$ mM, $\lambda_d \approx 10$ nm with $c^* = 1$ mM, $\lambda_d \approx 3$ nm with $c^* = 10$ mM, and $\lambda_d \approx 1$ nm with $c^* = 100$ mM. Estimates of the

Debye layer thickness should be carefully considered when selecting both the size of the system to use and the range of solutes that will be present in the system, because the analysis here relies on the assumption that $\lambda_d/h_1 \ll 1$.

Lubrication approximation

In this section, we consider the limit of a long, narrow pore ($\varepsilon_1 \ll 1$ and $\varepsilon_2 \ll 1$) and apply the lubrication approximation to simplify the governing equations to a tractable form. Effectively, this procedure reduces to a lubrication calculation of a pipe flow with slip, with the distinguishing feature that the slip boundary condition can be explicitly specified as a function of the dissolved solute concentration, the dynamics of which are also coupled to the fluid dynamics through the advection–diffusion equation given by Eq. (2e).

We assume $\varepsilon_1 < \varepsilon_2$, and so $\varepsilon_2 \ll 1$ guarantees $\varepsilon_1 \ll 1$. To proceed, we perform a perturbation expansion with the small parameter $\varepsilon_2 = h_2/L$ (we assume $0 \le h_1/h_2 \le 1$ for simplicity without loss of generality) for the limit of small pore Reynolds numbers $\mathrm{Re} \ll 1$:

$$u(x,y,z) = u_0(x,y,z) + \varepsilon_2^2 u_1(x,y,z) + \varepsilon_2^4 u_2(x,y,z) + \ldots \tag{4a}$$

$$v(x,y,z) = v_0(x,y,z) + \varepsilon_2^2 v_1(x,y,z) + \varepsilon_2^4 v_2(x,y,z) + \ldots \tag{4b}$$

$$w(x,y,z) = w_0(x,y,z) + \varepsilon_2^2 w_1(x,y,z) + \varepsilon_2^4 w_2(x,y,z) + \ldots \tag{4c}$$

$$p(x,y,z) = p_0(x,y,z) + \varepsilon_2^2 p_1(x,y,z) + \varepsilon_2^4 p_2(x,y,z) + \ldots \tag{4d}$$

$$c(x,y,z) = c_0(x,y,z) + \varepsilon_2^2 c_1(x,y,z) + \varepsilon_2^4 c_2(x,y,z) + \ldots \tag{4e}$$

Substituting Eqs. (4) into the governing Eqs. (2) and making the additional assumption that $\mathrm{Pe}\,\varepsilon_1^2 \ll 1$ gives to leading order

$$\frac{\partial^2 u_0}{\partial y^2} + \frac{h_1^2}{h_2^2}\frac{\partial^2 u_0}{\partial z^2} - \frac{\mathrm{d}p_0}{\mathrm{d}x} = 0, \tag{5a}$$

$$\frac{\partial p_0}{\partial y} = \frac{\partial p_0}{\partial z} = 0, \tag{5b}$$

$$\frac{\partial u_0}{\partial x} + \frac{\partial v_0}{\partial y} + \frac{\partial w_0}{\partial z} = 0, \tag{5c}$$

$$\frac{\partial^2 c_0}{\partial y^2} + \frac{h_1^2}{h_2^2}\frac{\partial^2 c_0}{\partial z^2} = 0. \tag{5d}$$

Integrating Eq. (5d) and applying the no-flux boundary conditions at the pore walls gives that $c_0 = c_0(x)$. With this result, Eq. (2e) becomes to the next leading order

$$\mathrm{Pe}\,u_0\frac{\mathrm{d}c_0}{\mathrm{d}x} = \frac{\mathrm{d}^2 c_0}{\mathrm{d}x^2} + \frac{\partial^2 c_1}{\partial z^2} + \frac{h_2^2}{h_1^2}\frac{\partial^2 c_1}{\partial y^2}. \tag{6}$$

Integrating over the pore cross section A, which is independent of x, and using the fact that at leading order

$$\frac{1}{A}\iint\limits_A u_0 \mathrm{d}A = 1, \quad \iint\limits_A \frac{\partial^2 c_1}{\partial y^2}\mathrm{d}A = 0, \quad \text{and} \quad \iint\limits_A \frac{\partial^2 c_1}{\partial z^2}\mathrm{d}A = 0, \tag{7}$$

then Eq. (6) simplifies to

$$\mathrm{Pe}\frac{\mathrm{d}c_0}{\mathrm{d}x} = \frac{\mathrm{d}^2 c_0}{\mathrm{d}x^2}. \tag{8}$$

Thus, the leading-order solute concentration satisfying the boundary conditions $c_0(0) = 1$ and $c_0(1) = \beta$ is given by

$$c_0(x) = \frac{\beta - 1}{\mathrm{e}^{\mathrm{Pe}} - 1}\left(\mathrm{e}^{\mathrm{Pe}x} - 1\right) + 1, \tag{9}$$

and the leading-order wall slip velocity, Eq. (3), is given by

$$u_w(x) = -\frac{\Gamma_w(x)}{L\bar{U}}\,\frac{\mathrm{Pe}\,(\beta - 1)\,\mathrm{e}^{\mathrm{Pe}x}}{\mathrm{e}^{\mathrm{Pe}} + (\beta - 1)\,\mathrm{e}^{\mathrm{Pe}x} - \beta}. \tag{10}$$

With additional information describing how the diffusioosmotic mobility varies with the solute concentration (and thus with the axial position x through Eq. (9)), this result for $u_w(x)$ can be used to solve Eq. (5a) for the axial fluid velocity and pressure within the pore.

Series solution

To solve Eq. (5a) for $u_0(x,y,z)$ and $p_0(x)$ subject to the boundary conditions previously described with $u_w(x)$ given by Eq. (10), we first write the axial velocity component as

$$u_0(x,y,z) = \frac{\mathrm{d}p_0}{\mathrm{d}x}\left(u_h(y,z) + \frac{1}{2}\left(y^2 - 1\right)\right) + u_w(x). \tag{11}$$

This representation satisfies Eq. (5a) when $u_h(y,z)$ satisfies the homogeneous equation

$$\frac{\partial^2 u_h}{\partial y^2} + \frac{h_1^2}{h_2^2}\frac{\partial^2 u_h}{\partial z^2} = 0, \tag{12}$$

subject to the boundary conditions $u_h = 0$ at $y = \pm 1$ and $u_h = \frac{1}{2}\left(1 - y^2\right)$ at $z = \pm 1$. Eq. (12) has a well-known series solution that can be found in classical references (see for example chapter 3 of White and Corfield[33]):

$$u_h(y,z) = \sum_{n=1}^{\infty} (-1)^{\frac{n-1}{2}} \frac{16}{n^3\pi^3} \cos\left(\frac{n\pi}{2}y\right) \frac{\cosh\left(\frac{n\pi}{2}\frac{h_2}{h_1}z\right)}{\cosh\left(\frac{n\pi}{2}\frac{h_2}{h_1}\right)}, \quad \text{for } n \text{ odd.} \tag{13}$$

To solve for the fluid pressure, consider the conservation of mass statement given by Eq. (7a). Using Eq. (11), we find

$$\frac{\mathrm{d}p_0}{\mathrm{d}x} = \frac{u_w(x) - 1}{\frac{1}{3} - C^*}, \tag{14}$$

where C^* is a well-known geometrical shape factor that depends on the pore aspect ratio h_1/h_2 and is given by

$$C^* = \frac{1}{A}\iint\limits_A u_h \mathrm{d}A = \sum_{n=1}^{\infty} \frac{64}{n^5\pi^5}\frac{h_1}{h_2}\tanh\left(\frac{n\pi}{2}\frac{h_2}{h_1}\right), \quad \text{for } n \text{ odd.} \tag{15}$$

Finally, if the diffusioosmotic mobility is known as a function of the solute concentration, then $\Gamma_w(x)$ is known, and the axial velocity profile in the pore is fully specified by Eq. (11). The pressure drop across the pore can then be determined by integrating Eq. (14). In the following sections, we apply this methodology to four cases: (1) electrolyte solutes with constant zeta potential, (2) electrolyte solutes with variable zeta potential, (3) non-electrolyte solutes with generic interactions, and (4) non-electrolyte solutes with purely steric interactions.

Electrolyte solutes with constant zeta potential

First, consider the case of constant zeta potential, where ζ is approximately uniform over the range of concentrations present in the system. This assumption will typically require that the ratio of solute concentrations in the system is not too large (i.e. β is close to one) and/or the absolute solute concentrations in the system are small. In this case, Γ_w can be assumed independent of x, and Eq. (14) can be directly integrated using Eq. (10) to give

$$p_0(x) = p_c + \frac{x + \frac{\Gamma_w}{L\bar{U}} \ln\left[\mathrm{e}^{\mathrm{Pe}} + \mathrm{e}^{\mathrm{Pe}x}(\beta - 1) - \beta\right]}{C^* - \frac{1}{3}}, \tag{16}$$

where p_c is a constant. Since we are dealing with incompressible flow, we have freedom in where we evaluate this constant. To facilitate comparison between pressure profiles, we choose $p = 0$ at $x = 1$, which gives

$$p_c = \frac{3}{1 - 3C^*}\left(1 + \frac{\Gamma_w}{L\bar{U}} \ln\left[\left(\mathrm{e}^{\mathrm{Pe}} - 1\right)\beta\right]\right). \tag{17}$$

Finally, the pressure drop across the pore $\Delta p = p(1) - p(0)$ is given by

$$\Delta p = \frac{3}{3C^* - 1}\left(1 + \frac{\Gamma_w}{L\bar{U}} \ln\beta\right), \tag{18}$$

where the second term in parentheses is the correction due to diffusioosmosis.

Thus, the pressure drop across the pore is uniquely specified by the solute concentration ratio β, the channel aspect ratio h_1/h_2 (through C^*), and the dimensionless diffusioosmotic mobility of the pore walls $\frac{\Gamma_w}{L\bar{U}}$. For a typical system, h_1/h_2, L, and β will be known parameters, and $\bar{U}$ and Δp can be experimentally measured. This situation could be modified, for example, if a sensitive pressure pump were used to maintain a fixed Δp along the pore, in which case only $\bar{U}$ would need to be measured. In any case, Eq. (18) can then be used to directly calculate the diffusioosmotic mobility of the pore walls. Finally, if corrections due to finite Debye layer effects can be neglected, ζ can be found by solving

$$\Gamma_w = \frac{\varepsilon}{\mu}\left(\frac{k_B T}{Ze}\right)^2 \left[\left(\frac{D_+ - D_-}{D_+ + D_-}\right)\frac{Ze\zeta}{k_B T} + 4\ln\cosh\left(\frac{Ze\zeta}{4k_B T}\right)\right], \tag{19}$$

where ε is the permittivity of the medium, μ is the dynamic viscosity of the medium, k_B is the Boltzmann constant, T is the temperature, Z is the valence of the Z–Z solute, e is the elementary charge, and D_+ and D_- are the diffusivities of cations and anions, respectively[13].

Electrolyte solutes with variable zeta potential

While the case of constant ζ is convenient in that it results in the analytical relation given by Eq. (18), the assumptions of β close to one and/or small solute concentrations are probably not realistic for the purposes of zeta potentiometry in some systems. Although the assumption of constant ζ is frequently found in the literature and is theoretically justifiable for the case of low solute concentrations[32,34], in our system, β close to one will result in weak diffusioosmosis, requiring flow rate and pressure drop measurements with impractical sensitivity. Furthermore, at electrolyte concentrations low enough for ζ to be treated as constant, finite Debye layer effects would almost certainly invalidate the approximate wall slip boundary condition assumed in our model. Thus, in this section we consider the use of this system when ζ is variable.

Kirby and Hasselbrink Jr. suggest that ζ is proportional to the logarithm of the solute concentration for the case of symmetric electrolytes with a valence of one for a wide range of solute concentrations.[34] Specifically, if the cations do not show specific adsorption, the zeta potential is given approximately by

$$\zeta = -a_1 \ln c^*, \tag{20}$$

where a_1 is a constant of proportionality, and c^* is expressed in M.[34] For more details on when the form of Eq. (20) can be expected to hold, see Kirby and Hasselbrink Jr.[34] Modified relationships analogous to Eq. (20) can also be found for other situations when the electrolyte is not 1–1.[34]

For the case of variable zeta potential, there is no longer a single ζ value present in the system, since the solute concentration varies throughout the pore. However, with the assumptions described above, the interface can still be described by a single free parameter, the constant of proportionality a_1, which describes how the zeta potential varies with solute concentration. The determination of a_1 can be achieved as follows. First, Γ_w can be written explicitly as a function of x by substituting Eq. (9) into Eq. (20) and substituting Eq. (20) into Eq. (19), where the only unknown is a_1. Next, Eq. (10) can be rewritten with the now-variable $\Gamma_w(x)$ to give a new analytical form for the wall slip velocity as an explicit function of x. With $u_w(x)$ given as a more-complicated expression that includes a dependence on a_1, the pressure gradient along the pore once again satisfies Eq. (14), although analytical integration becomes intractable due to the complicated functional dependence of u_w on x. However, numerical integration remains viable, and a shooting procedure in the unknown variable a_1 can be used until the numerically integrated pressure drop across the pore matches the measured experimental values.

Non-electrolyte solutes with generic interactions

Next, we consider the case of non-electrolyte solutes with unknown interaction potentials. The diffusioosmotic flow over a flat surface due to non-electrolyte gradients is given by[21,22,28]

$$u_w = -\frac{L^* \Gamma k_B T}{\mu L\bar{U}}\frac{\mathrm{d}\ln c}{\mathrm{d}x} = -\frac{L^* K k_B T c^*(0)}{\mu L\bar{U}}\frac{\mathrm{d}c}{\mathrm{d}x}, \tag{21}$$

where

$$\Gamma = \int_0^\infty [c^*(y^*) - c^*_\infty]\,\mathrm{d}y^* \tag{22}$$

is the Gibbs surface excess of solute, $K = \Gamma/c^*$, $c^*(y)$ represents the variation of the solute concentration inside the diffuse layer, c^*_∞ represents the solute concentration sufficiently far from the surface, $c^*(0)$ is the reference solute concentration at $x = 0$, and

$$L^* = \frac{\int\limits_0^\infty y^* \left[\exp(-E/k_B T) - 1\right] \mathrm{d}y^*}{\int\limits_0^\infty \left[\exp(-E/k_B T) - 1\right] \mathrm{d}y^*} \tag{23}$$

is a characteristic length scale for the solute–surface interaction on the order of 10 to 100 Å, where $E(y)$ is the energy of a solute molecule a distance y from the surface, which typically is not known.[21] Following the notation of Eq. (3), the diffusioosmotic mobility for this case is given by

$$\Gamma_w(x) = \frac{k_B T}{\mu} L^*(x)\,\Gamma(x), \tag{24}$$

where the Gibbs surface excess of solute can be measured experimentally with material balances, but Anderson and Prieve suggest that L^* cannot be directly measured.[21] However, using our method, this interaction length scale can at least be approximated. If L^* is not too sensitive to the solute concentration, c^*, a relatively small ratio of solute concentrations can be selected (e.g. $\beta = 0.1$ or 10) and an effective L^*_{eff} can be assumed constant over that range. The dependence of L^*_{eff} can then be investigated by varying the absolute reference solute concentration and using a numerical shooting procedure as described in the previous section to calculate L^*_{eff}.

Non-electrolyte solutes with purely steric interactions

For certain types of non-electrolyte solute/surface interactions, additional theoretical progress can be made. For example, in this section we consider the case of purely steric exclusion interactions. Staffeld and Quinn showed that for steric interactions the Gibbs surface excess of solute is given by $\Gamma(x) = -r_\mathrm{I}\, c^*(x)$, and $L^* = \frac{r_\mathrm{I}}{2}$, where r_I is the interaction radius of the solute/surface interaction, i.e. the distance of closest approach of the solute to the surface.[22] Then for this case we have

$$u_w(x) = \frac{k_B T c^*(0)}{\mu L \bar{U}} \frac{\mathrm{e}^{\mathrm{Pe}x}\mathrm{Pe}(\beta-1)}{\left(\mathrm{e}^{\mathrm{Pe}}-1\right)} \frac{r_\mathrm{I}^2}{2}, \tag{25}$$

and integrating Eq. (14) gives

$$p_0(x) = p_c + \frac{3}{1-3C^*}\left(\frac{k_B T c^*(0)}{2\mu L \bar{U}} \frac{\mathrm{e}^{\mathrm{Pe}x}(\beta-1)}{\left(\mathrm{e}^{\mathrm{Pe}}-1\right)} r_\mathrm{I}^2 - x\right), \tag{26}$$

where

$$p_c = \frac{3}{1-3C^*}\left(1 - \frac{k_B T c^*(0)}{2\mu L \bar{U}} \frac{\mathrm{e}^{\mathrm{Pe}}(\beta-1)}{\mathrm{e}^{\mathrm{Pe}}-1} r_\mathrm{I}^2\right). \tag{27}$$

Finally, the pressure drop across the pore is given by

$$\Delta p = \frac{3}{1-3C^*}\left(\frac{k_B T c^*(0)}{2\mu L \bar{U}} (\beta-1) r_\mathrm{I}^2 - 1\right). \tag{28}$$

Thus, as with the case of electrolyte solutes with constant zeta potential, here we find a simple analytical result relating the pressure drop and flow velocity in the pore with the representative parameter that characterizes the surface/solute interaction, in this case the interaction radius r_I for non-electrolyte solutes with purely steric interactions.

Summary

Thus, for the cases of electrolyte solutes with constant ζ and non-electrolyte solutes with purely steric interactions, our method provides simple analytical results given by Eq. (18) and Eq. (28) that can be used to estimate the zeta potential or interaction radius, respectively, through pressure drop and flow rate measurements. For the remaining cases of electrolyte solutes with variable ζ and non-electrolyte solutes with other interaction potentials, our method provides a numerical shooting method that can be used to measure the proportionality constant a_1 in Eq. (20) or the effective characteristic interaction length scale L^*_{eff}, respectively, once again based on pressure drop and flow rate measurements in the pore. Note that this numerical procedure described for variable ζ is generally more practical because the assumptions needed to neglect variations in ζ, e.g. $\beta \approx 1$ and/or $c^* \ll 1$ result in weak diffusioosmosis and/or finite Debye layer effects which invalidate the approximation of the diffusioosmosis as a wall slip boundary condition. In the next section, we use three-dimensional numerical simulations to validate the theoretical results presented above for the example case of electrolyte solutes with constant zeta potential, and we show that the end effects due to the pore/side-channel junctions are negligible for many practical system parameters of interest.

Numerical simulations

In this section we use 3D numerical simulations of the governing equations given by Eq. (2), which include the steady, incompressible Navier-Stokes and continuity equations, as well as the advection–diffusion equation governing the solute concentration dynamics, to verify the theory presented in the previous section. We will use the case of electrolyte solutes with constant ζ for ease of comparison with the analytical result given by Eq. (18). In deriving our theory, we assumed that the solute concentrations at the pore inlet and outlet are uniform across the cross-section and equal to the solute concentration in the corresponding main channel, i.e. $c = 1$ at $x = 0$ and $c = \beta$ at $x = 1$. However, this assumption requires verification, because end effects due to advection and diffusion in the main channel flows certainly affect the solute concentrations near the pore inlet and outlet. For example, according to Eq. (10), the diffusioosmotic outflow velocity at $x = 1$ is proportional to β^{-1} for $\beta \ll 1$. Thus, decreasing β leads to a stronger outflow of the relatively higher solute concentration flow in the pore into the main channel. This increases the effective value of β (for $0 < \beta < 1$) at the pore outlet from that expected by our theory, and thus the measured outflow velocity will be less than expected, and the corresponding measured pressure drop will likewise be affected. Thus, in order for such a system to be useful in practice, we must first determine under what conditions these end effects will be negligible.

In order to validate the theory presented in the previous section

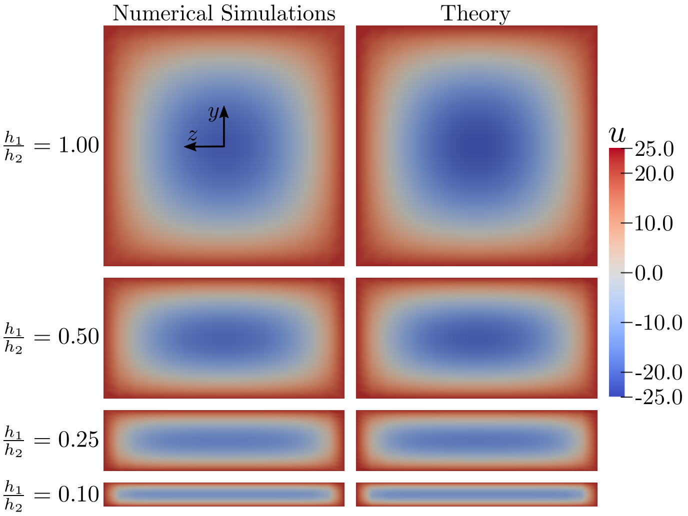

Fig. 2 Comparison of the axial velocity profiles u for the three-dimensional numerical simulations and the theoretical predictions given by Eq. (11) for a variety of channel aspect ratios h_1/h_2. Results are taken at $x = 0.99$ for $\beta = 0.01$, $Pe = 1$, $\varepsilon_2 = 5 \times 10^{-4}$, $\Gamma_w/L\bar{U} = 0.375$, and $\mathrm{Re} = 8.89 \times 10^{-7}$, 4.44×10^{-7}, 2.22×10^{-7}, and 8.89×10^{-8} from top to bottom. With $\beta < 1$ and $\Gamma_w/L\bar{U} > 0$, the maximum diffusioosmotic effects occur in the vicinity of the pore outlet. Here, we see that at $x = 0.99$ the wall slip velocity is nearly 25 times larger than the mean pore speed $\bar{U}$. This strong outflow necessitates a reversal of flow along the pore centerline to conserve mass flux along the pore. As can be seen, numerical results agree well with the theoretical predictions, suggesting that even at $x = 0.99$ the end effects at the pore outlet are negligible.

and to quantify the impact of end effects, numerical simulations were performed using the open-source computational fluid dynamics toolbox OpenFOAM.[35] Details of the numerical methods used and of the simulation mesh design are given in Appendix B. To validate the theory presented in the previous section, we first compare numerical results for the axial velocity near the pore outlet with the theoretical predictions given by Eq. (11) for a variety of channel aspect ratios $\frac{h_1}{h_2}$ with $\beta = 0.01$, $\mathrm{Pe} = 1$, and $\frac{\Gamma_w}{L\bar{U}} = 0.375$, which are experimentally plausible[7]. Results are presented in Figure 2 at $x = 0.99$, where the wall slip velocity is found to be approximately 25 times greater than the average axial flow velocity. This outflow in turn drives an inflow along the pore centerline to conserve mass. Despite these relatively large velocities near the pore outlet, end effects are apparently negligible, even at $x = 0.99$. Centerline pressures along the pore for these cases are compared with the theoretical predictions of Eq. (16) in Figure 3. As mentioned, p_c was chosen such that $p = 0$ at $x = 1$ for the theoretical prediction. As can be seen in the figure inset, deviations from the theoretical predictions do occur in the very near vicinity of the pore outlet due to the end effects. However, we will show in the next paragraph that when comparing total pressure drops along the pore between the numerical simulation data and the theoretical predictions, these end effects do not cause significant errors for many practical choices of system parameters.

We compare the numerically computed pressure drops along the pore with the theoretical predictions given by Eq. (18) for a variety of dimensionless solute concentration ratios β and wall diffusioosmotic mobilities $\frac{\Gamma_w}{L\bar{U}}$ in Figure 4. Results were computed

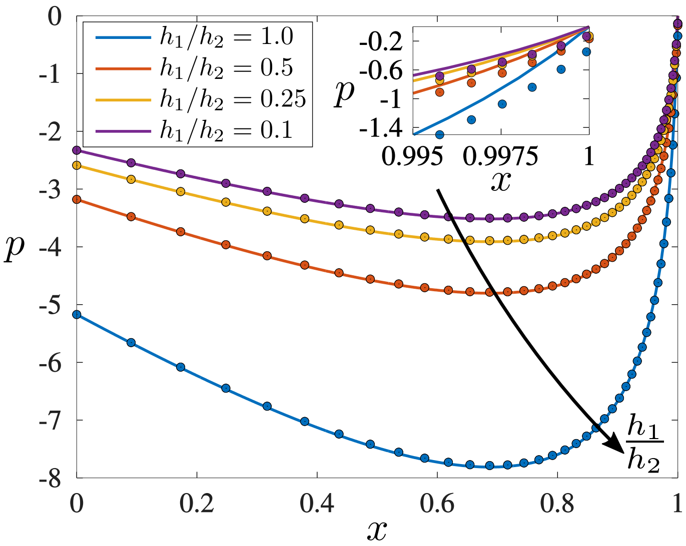

Fig. 3 Pore pressure profiles for a variety of channel aspect ratios h_1/h_2 with $Pe = 1$, $\Gamma_w/L\bar{U} = 0.375$, $\beta = 0.01$, $\varepsilon_2 = 5 \times 10^{-4}$, and $\mathrm{Re} = 8.89 \times 10^{-8}$, 2.22×10^{-7}, 4.44×10^{-7}, and 8.89×10^{-7}. Solid lines correspond to the theoretical predictions given by Eq. (16), and symbols correspond to the results of the 3D numerical simulations. For visualization purposes, numerical results were shifted such that $p_{\text{num}} = p_{\text{theory}}$ at $x = 0$. As can be seen, the maximum pressure drop $\Delta p = p(x = 1) - p(x = 0)$ is achieved with a square channel $h_1/h_2 = 1$, which is intuitive since increasing h_2 for a fixed h_1 effectively increases the hydraulic diameter of the channel, reducing the necessary pressure gradient to drive the flow. The figure inset shows the pressure profiles near the pore outlet, where end effects begin to cause relatively small deviations from the theoretical predictions.

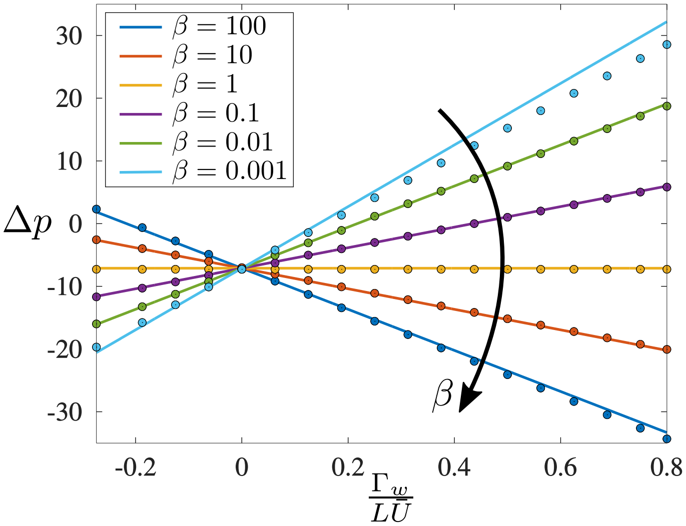

Fig. 4 Pressure drop across the pore $\Delta p = p(x = 1) - p(x = 0)$ as a function of the wall diffusioosmotic mobility $\Gamma_w/L\bar{U}$ for a variety of nondimensional solute concentration ratios β with $h_1/h_2 = 1$, $Pe = L\bar{U}/D_s = 1$, $\varepsilon_1 = \varepsilon_2 = 5 \times 10^{-4}$, and $\mathrm{Re} = 8.89 \times 10^{-7}$. Solid lines are theoretical predictions of Eq. (18), and symbols are results of 3D simulations. For modest solute concentration ratios, the simulations agree well with the theoretical predictions. However, for $\beta = 0.001$ we start to observe deviations from the theoretical results as the end effects apparently are significant. The wall slip boundary condition at the pore junction $u_w(x = 1) \propto \beta^{-1}$ for $\beta \ll 1$. Thus, decreasing β increases the outflow velocity, which carries the higher solute concentration fluid out into the main channel, effectively increasing the solute concentration at the pore outlet. This increases the effective β value, decreasing the pressure gradient along the pore.

for a solute Peclet number $\mathrm{Pe} = 1$ with a pore aspect ratio $h_1/h_2 = 1$. The range of $\frac{\Gamma_w}{L\bar{U}}$ shown in the figure roughly corresponds to a physically realistic range of system parameters. As can be seen, for a wide range of solute concentration ratios and wall surface charges, Eq. (18) accurately predicts the dimensionless pressure drop Δp along the pore. These results suggest that the type of flow systems described here and shown graphically in Figure 1 may be designed such that end effects can be minimized, and the measured pressure drop across the pore can provide an accurate measure of the diffusioosmotic mobility of the pore walls, and thus a measure of the surface's zeta potential.

Comparison with previous data

In this section, we apply the methods presented above to the experimental results of Lee *et al.*[1], and we propose several modifications to their experimental design that will facilitate the use of such a system for the purposes of zeta potentiometry. Lee *et al.* provided experimental evidence of convective fluid motion in a solute gradient due to diffusioosmosis, and they presented a theoretical analysis of this transport phenomenon.[1] They fabricated H-shaped channels similar to the geometry in Figure 1 with $L = 150\ \mu$m, $2h_1 = 163$ nm, and $2h_2 = 5\ \mu$m using conventional nanofabrication techniques with Si chips. As described above, they applied different electrolyte solute concentrations to each end of the pore in order to induce diffusioosmosis. They took special care to eliminate any pressure-driven flow inside the pore in order to isolate the diffusioosmotic effects. They were able to measure the flow rate in the pore with a sensitivity of about 50 fl/min, and by varying the applied solute concentrations they observed both positive and negative flow rates in the pore.

Lee *et al.* plotted the results for their measured flow rates versus the logarithm of the concentration ratio between the pore inlet and outlet in their Figure 2.[1] They also presented in their Equation (3) a linear relationship between the flow rate and the concentration ratio, albeit without a rigorous derivation. This result is equivalent to a special case of our Eq. (18) for the case $\Delta p = 0$. Note that, while this special case is valuable for the purposes of isolating the diffusioosmotic effects, which was the goal of Lee *et al.*, several special considerations are needed to adapt their system for the purposes of zeta potentiometry as described here. For example, in order to minimize spurious residual convection, Lee *et al.* apparently insulated their system by unplugging all tubings and sealing the ports prior to their experiments.[1] That is, they apparently set $\bar{U}_{\mathrm{main},1} = \bar{U}_{\mathrm{main},2} = 0$ and allowed the system to settle before performing their measurements. While this has the desired effect of eliminating spurious pressure-driven flow in the pore, the flow in the main side channels serves the useful purpose of maintaining the solute boundary conditions at the ends of the pore, and as we have shown, end effects must be considered. Thus, we do not recommend attempting to set $\Delta p = 0$ for the purposes of zeta potentiometry. Rather, we suggest that steady flow in the main channels be maintained throughout the experiment and the pressure drop across the pore be directly measured in order to mitigate end effects.

Using three different solutes: KI, NaI, and LiI, Lee *et al.* measured flow rates in the range of ±500 fl/min with solute concentration ratios ranging from about $\beta = 0.1$–10 and typical velocities on the order of 1–10 μm/s.[1] Using the experimental flow rate measurements presented in their Figure 2, we first estimate the corresponding zeta potential predictions for each of their data points based on the initial assumption of constant ζ (which is an assumption they also made). These values are presented in Figure 5, where the error bars correspond to the uncertainty in their flow rate measurements of ±50 fl/min. These values were computed by first applying Eq. (18) to calculate the diffusioosmotic mobilities, and then solving Eq. (19) for the corresponding zeta potential assuming a temperature of $T = 20°$C. Lee *et al.* also used a standard electroosmotic measurement technique at a solute concentration of 10 mM to measure the surface charge of their channels, which they estimated as $\zeta = -85 \pm 2$ mV.[1]

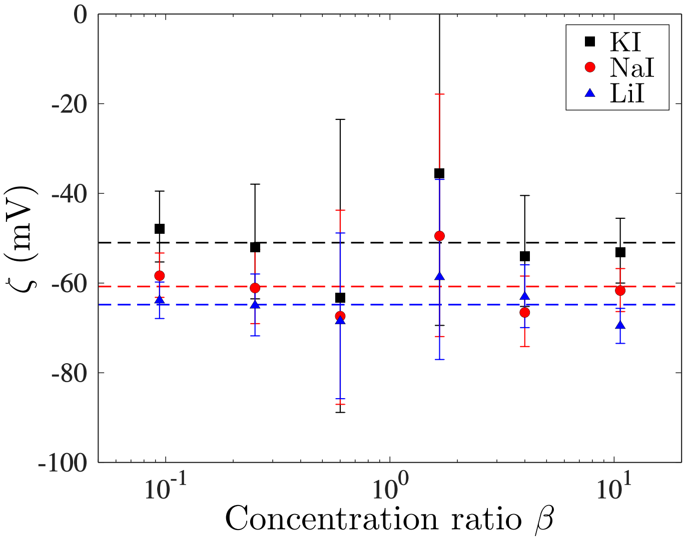

Fig. 5 Calculated zeta potential values based on the experimental flow rate versus solute concentration ratio measurements presented in Figure 2 of Lee *et al.*[1] based on the assumption of uniform zeta potential and with $\Delta p = 0$. Error bars are based on the sensitivity of their flow rate measurements of ±50 fl/min. Results under-predict the magnitude of the zeta potential relative to their electroosmotically measured value of $\zeta = -85 \pm 2$ mV, where the error increases with the ambipolar diffusivity of the solute.

Note that the zeta potential predictions based on the diffusioosmotic theory predictions shown in Figure 5 under-predict the magnitude of the zeta potential relative to their electroosmotic measurement, and furthermore, the results show some variability between the different solutes. There are several potential explanations for these behaviors. First, the electroosmotic measurement reported by Lee *et al.*[1] is taken at a fixed solute concentration of 10 mM, whereas in the diffusioosmosis experiments the solute concentration varies by about one order of magnitude throughout the channel. Thus, variability of the zeta potential throughout the system may be a factor, which we will investigate shortly. Second, the diffusioosmosis theory makes the assumption of infinitesimal Debye layer thickness relative to the channel size. However, with Debye lengths up to 10 nm at the solute concentrations used in their system, finite Debye layer effects may play a role in their 163 nm thick channels with values of λ_d/h_1

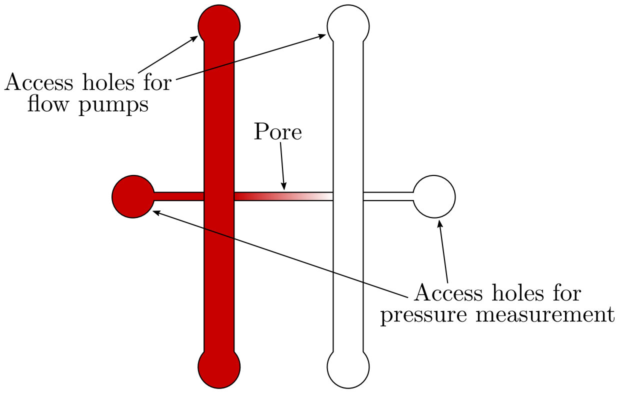

Fig. 6 Sample experimental design for zeta potential measurement. By extending the pore through the main side channels, pressure ports can be added to measure the pressure drop across the pore. Validation simulations suggest that the pressures experienced within the access holes for pressure measurement are approximately equal to the pressures at the corresponding end of the pore for typical system parameters.

up to approximately 1/8. Furthermore, steric effects due to the different-sized ions may play a role in the variability seen across solutes, although this effect should be negligible at the concentrations seen in their experiments.

However, the most significant source of error for the diffusioosmotic measurements likely arises from the fact that Lee *et al.*[1] set $\Delta p = 0$ in order to isolate the diffusioosmosis. With no flow in the main side channels of the system, the solute boundary conditions at the inlet and outlet of the pore are not strictly maintained. The effective solute concentration at the end of the pore corresponding to the low solute concentration will be higher than expected, and the effective solute concentration at the end of the pore corresponding to the high solute concentration will be lower than expected. The net effect of this is that the pore will see a smaller solute concentration gradient than expected, resulting in weaker diffusioosmosis and a smaller predicted magnitude for the diffusioosmotic mobility and zeta potential. This behavior is corroborated by the data shown in Figure 5, as the magnitude of the predicted zeta potentials tends to decrease as the ambipolar diffusivity of the solute increases. The ambipolar diffusivities $D_s = 2D_+D_-/(D_+ + D_-)$ of the given salts are $D_s \approx 2.00 \times 10^{-9}$ m^2/s, $D_s \approx 1.61 \times 10^{-9}$ m^2/s, and $D_s \approx 1.37 \times 10^{-9}$ m^2/s for KI, NaI, and LiI, respectively. The solution to this source of error is to maintain a continuous flow rate in the main side channels and directly measure the pressure drop across the pore. To do so, a simple modification of the experimental design of Lee *et al.*[1] is to extend the pore through the side main channels and provide access ports for pressure measurements as shown in Figure 6.

Finally, we consider the role of variable zeta potential in this system. As mentioned above, using standard electroosmotic measurement techniques, Lee *et al.* estimated the zeta potential of their channels to be $\zeta = -85 \pm 2$ mV at a solute concentration of 10 mM.[1] Thus, using Eq. (20), the proportionality constant a_1 for their system can be estimated as $a_1 = -18.5$ mV. Using this value, the solute concentration, zeta potential, and diffusioosmotic mobility profiles throughout the pore are shown in Figure 7 for the solute concentrations used by Lee *et al.*[1], assuming that the solute concentration boundary conditions at the pore ends were well-maintained by steady flow in the main side channels. These results demonstrate that relatively large variations in both the zeta potential and diffusioosmotic mobility are present in Lee *et al.*'s experiments, and the assumption of uniform zeta potential made by Lee *et al.*[1] and needed for the application of Eq. (18) is not likely valid at these combinations of absolute solute concentration and solute concentration ratios. This variability represents an additional source of error in the estimates of zeta potential provided in Figure 5. These errors due to variable ζ can be simply eliminated by using the numerical procedure outlined in the *Electrolyte solutes with variable zeta potential* section. For most practical systems, the use of Eq. (18) should generally be restricted to the use of making quick predictions about the effective diffusioosmotic mobility or zeta potential of the channel walls.

Typical experimental parameters and uncertainty

Finally, in this section we suggest typical experimental parameters that may be used to minimize the various potential sources of error that may be present in the system. First, we will suggest the use of a $0.4 \times 5 \times 150$ μm^3 pore. By using a taller channel (400 nm versus 163 nm as in Lee *et al.*[1]) the approximation of the diffusioosmosis as a wall slip boundary condition will be better satisfied. With Debye lengths less than 10 nm at solute concentrations above 1 mM, finite Debye layer effects should be negligible. In order to select the solute concentrations to use, several considerations must be evaluated. First, assuming a given sensitivity for the measurement of the flow rate (e.g. 50 fl/min in Lee *et al.*[1]), a larger ratio of high to low solute concentrations gives a better sensitivity in the zeta potential measurement as seen in Figure 5. However, too large of an applied solute concentration ratio will result in a breakdown of the pore end solute concentration boundary conditions, as shown in Figure 4. A choice of $\beta = 0.01$ or 100 appears to be a reasonable choice. For these values it will be necessary to apply the method previously described for variable diffusioosmotic mobility. The form of the zeta potential given by Eq. (20) is valid for silica below solute concentrations of 100 mM at pH > 6 and below 10 mM at pH > 3.5. Thus, we recommend the use of solute concentrations of 1 mM and 100 mM in the two main channels for pH > 6 and 0.1 mM and 10 mM for $6 > \text{pH} > 3.5$.

All that remains is to estimate the uncertainty in the measurement technique. As an order-of-magnitude estimate, we consider the result of Eq. (18), which can be solved for Γ_w as

$$\Gamma_w = \frac{(3C^* - 1)\, h_1^2 \,\Delta p^* - 3L\bar{U}\mu}{3\mu \ln\beta}, \tag{29}$$

where Δp^* is the dimensional pressure drop across the pore. Then, considering δp^* and $\delta \bar{U}$ the uncertainties in the pressure drop and mean velocity measurements, respectively, the uncertainty in the diffusioosmotic mobility coefficient $\delta\Gamma_w$ is approximately

$$\delta\Gamma_w = \sqrt{\left(\frac{\partial \Gamma_w}{\partial \Delta p^*}\delta p^*\right)^2 + \left(\frac{\partial \Gamma_w}{\partial \bar{U}}\delta \bar{U}\right)^2}, \tag{30}$$

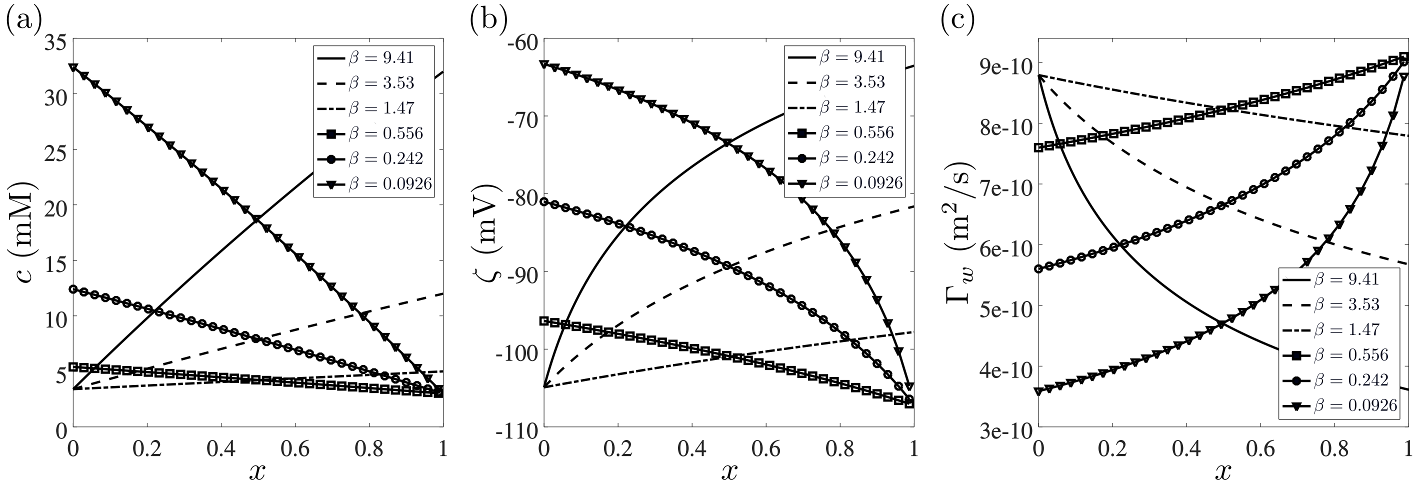

Fig. 7 Predicted solute concentration, zeta potential, and diffusioosmotic mobility coefficient profiles for the experimental solute concentration ratios from Lee *et al.* [1] using their electroosmotically measured value of $a_1 = -18.5$ mV. Results demonstrate the wide variation of both ζ and Γ_w along the pore, suggesting that the assumptions of constant zeta potential and diffusioosmotic mobility are not valid at the solute concentrations seen in Lee *et al.*'s experiments. Thus, in addition to diffuse, transient solute boundary conditions at the pore ends, zeta potential variability represents another source of error for the predictions of Figure 5, and in general the procedure we outlined in the *Electrolyte solutes with variable zeta potential* section should be utilized instead of Eq. (18), except perhaps in the dilute limit.

which simplifies to

$$\delta\Gamma_w = \sqrt{\left(\frac{(3C^*-1)\,h_1^2}{3\,\mu\ln\beta}\delta p^*\right)^2 + \left(\frac{L}{\ln\beta}\delta\bar{U}\right)^2}. \qquad (31)$$

Using the same strategy as Lee *et al.* [1] to measure flow rate, an uncertainty in the mean flow speed of approximately $\delta\bar{U} = 1$ μm/s can be achieved, and with high-precision pressure sensors, an uncertainty of $\delta p^* = 10$ Pa is possible. Then, with the channel geometry and solute concentration ratios suggested above, the uncertainty in diffusioosmotic mobility coefficient is on the order of $\delta\Gamma_W \sim 1\times10^{-10}$ m^2/s. By varying the flow rates in the side channels, multiple measurements with different $\bar{U}$ and Δp^* can be performed to improve the accuracy of the final measurement.

Conclusion

We have proposed a novel microfluidic technique for measuring these properties for solid surfaces using diffusioosmosis. By introducing two fluids with different solute concentrations into two main channels connected by a long, narrow pore, a steady-state solute concentration gradient is established within the pore. Due to solute–surface interactions, this solute concentration gradient can drive a diffusioosmotic wall slip boundary condition on the channel walls within the pore, which in turn result in predictable deviations of the fluid velocity and pressure profiles from the well-known Poiseuille flow. These deviations allow theoretical relationships to be developed between the pressure drop across the pore, the mean flow speed in the pore, and the diffusioosmotic mobility coefficient of the channel walls.

For the cases of electrolyte solutes with constant ζ and non-electrolyte solutes with purely steric interactions, we derived simple analytical results that can be used to predict the zeta potential and interaction radius, respectively, for the two cases based on pressure drop and flow rate measurements. For the more general cases with electrolyte solutes with variable ζ and non-electrolyte solutes with other interaction potentials, we presented a numerical method that can be used to predict the proportionality constant a_1 and the effective characteristic interaction length L^*_{eff}, respectively, for the two cases also based on pressure drop and flow rate measurements. We used 3D numerical simulations of the coupled governing equations to validate the theoretical results for the test case of electrolyte solutes with constant ζ, and we confirmed that end effects are negligible for a wide range of parameters. Finally, we illustrated the use of our method by applying it to the experimental results of Lee *et al.* [1] and analyzed the various potential sources of error in the system. Our findings suggest that the surface–solute interactions of both electrolyte and non-electrolyte solutes with flat, solid surfaces can be characterized using diffusioosmosis, and so possibly eliminate the need for expensive and sophisticated electrical components.

Acknowledgments

We would like to thank Suin Shim for insightful conversations on the effects of variable zeta potential. HAS thanks the NSF via grant CBET-1702693. We greatly appreciate the valuable feedbacks of the anonymous reviewers that helped us to greatly expand and strengthen this manuscript.

Conflict of interest

The authors declare no conflicts of interest.

Appendix A: Review of other methods

In this section, we review several of the most common methods for measuring the zeta potential of surfaces, and we discuss potential limitations of the techniques that should be considered when selecting a measurement approach. Specifically, we discuss the electroosmosis method, the streaming potential method, the streaming current method, and the ZetaSpin method.

Electroosmosis method

The modern theory of electroosmosis was primarily developed by von Smoluchowski.[36] When an external electrical field is applied parallel to a solid–liquid interface, the field exerts an electrical body force on the excess counterions in the charged diffuse layer near the interface. As these ions are pulled by this field, they drag the liquid with them, resulting in an electroosmotic flow.[37] Depending on the geometry of the system, the Smoluchowski equation, which relates the electroosmotic mobility to the interface zeta potential, can be used to relate the zeta potential, the applied electric field, and the average flow velocity. Thus, the zeta potential can be determined simply by measuring the electroosmotic flow velocity in a system for a given applied field. Typically, the electroosmotic flow velocity $\boldsymbol{u}_{\text{eo}}$ due to an external applied electric field $\boldsymbol{E}_{\text{ext}}$ is given by:

$$\boldsymbol{u}_{\text{eo}} = -\frac{\varepsilon\zeta}{\mu}\boldsymbol{E}_{\text{ext}}, \tag{32}$$

where ε and μ are the permittivity and dynamic viscosity of the medium, respectively.

While theoretically straightforward, the electroosmotic approach does suffer from several limitations. First, electroosmosis measurements are often limited to a certain pH and solute concentration range in order to avoid damaging the electrodes in the system.[25] Furthermore, electroosmotic mobility measurements of ζ also suffer from errors due to Joule heating from the applied voltage; typical experiments have been reported to suffer from no less than 5-10 °C of heating, with ∼3% error per °C.[37,38] This heating limits the magnitude of the potential that can be applied, effectively reducing the electroosmotic flow velocity in the system. For this reason, some researchers prefer the streaming potential method over electroosmosis because it is sometimes more convenient to measure small electrical potentials than to measure small flow rates[39,40].

Nonetheless, the electroosmosis technique has been used with success. For example, Yan *et al.* demonstrated a novel use of micro particle image velocimetry to measure the temporal development of the electroosmotic flow in microchannels and showed that this technique can simultaneously determine the zeta potential of the channel walls and the electrophoretic velocity of tracer particles.[41] Another technique, developed by Corbett *et al.*, uses phase analysis light scattering to measure the mobility of tracer particles in the vicinity of a charged test surface in a dip cell arrangement, and a model of the electroosmotic flow near the surface allows the prediction of the surface's zeta potential.[42]

Furthermore, Sze *et al.* used a novel experimental technique that measured the slope of the current–time relationship in an electroosmotic flow with transient solute concentration and used the Smoluchowski equation to perform repeatable zeta potential measurements of glass and polydimethylsiloxane (PDMS) coated surfaces.[37] The authors claim that, because this approach uses electroosmotic flow, in contrast to the pressure-driven flows in streaming potential/current measurements, the electroosmosis measurements are more representative of the operating conditions of many microfluidic devices that use electroosmotic flows. There is a physical basis for this claim. When measuring the zeta potentials of plane ceramic membranes, a comparison between results from electroosmosis and streaming potential methods found that electroosmosis gives greater zeta-potential values.[25] These results suggest that the location of the shearing plane depends on which electrokinetic measurement method is used, and the choice of measurement method should be informed by the ultimate system of interest. That is, if the system of interest involves flows induced by external electrical potentials, one should consider using electroosmosis to measure the zeta potentials of the system, whereas if the system of interest involves flows induced by applied solute gradients, one should consider the diffusioosmotic method we propose here, since the physical, true zeta potential may be different in the two flows.[25,43]

Streaming potential method

Another, and more popular, technique for measuring the zeta potentials of solid surfaces exposed to electrolyte solutes is the streaming potential method. The electrical double layer carries a net charge due to the accumulated counterions near the interface. Thus, when a pressure gradient is applied to drive a flow, a streaming current results, leading to the build up of a potential difference, which in turn leads to a back conduction. When equilibrium is achieved, the back current and streaming current are equal, and the measured potential difference across the capillary or channel is the streaming potential.[40] In such a system, the zeta potential is given by the Helmholtz-Smoluchowski equation[40,44,45]:

$$\zeta = \frac{E_s}{\Delta p}\,\frac{\mu}{\varepsilon\varepsilon_0}\,\frac{L}{A}\,\frac{1}{R}, \tag{33}$$

where E_s is the induced streaming potential, Δp is the applied pressure difference along the channel, μ is the dynamic viscosity of the liquid, ε is the liquid permittivity, ε_0 is the permittivity in vacuum, R is the electrical resistance across the channel, L is the length of the channel, and A is the cross-sectional area of the channel. In Eq. (33), $E_s/\Delta p$ can be determined by direct measurement of the streaming potential for a given applied pressure difference, and R can be measured using an AC conductivity bridge.[40] The streaming potential method has been used successfully to measure the zeta potentials of reverse osmosis membranes[40], fused silica slides[46], granular porous media surfaces[26], and many other surfaces. Streaming potential measurements have also been used on commercial nanofiltration and reverse osmosis membranes to study the influence of solution chemistry on the zeta potential of membrane surfaces.[40,47–49]

While this method has proven reliable, streaming potential measurements still have several reported challenges. As with electroosmosis, streaming potential methods are also often limited to a certain pH range in order to avoid damaging the electrodes.[25,26] Furthermore, large pressures on the order of a few bars are typical for streaming potential techniques, which can require careful sealing of the system.[42] Another issue that must be considered in streaming potential measurements is asymmetric streaming potentials when the flow direction is reversed due to small differences in the electrode potential.[26,46] To overcome this issue, Ball and Fuerstenau suggest measuring the slope of the potential versus pressure drop relation as opposed to individual potential/pressure drop values.[23] Another complication to streaming potential measurements is the presence of finite surface conductivity, which can represent a non-negligible contribution to the total electrical conductivity. For example, in one study performing streaming potential measurements of granular porous media, the contribution of surface conductance to the total conductivity was 13.5% at an electrolyte concentration of 0.1 M, which increased to 69.4% at an electrolyte concentration of 10^{-5} M.[26]

Streaming potential measurements also rely on the assumptions of steady, incompressible, laminar, and fully developed flow, which may be limiting factors for some systems. For example, Van Wagenen and Andrade performed a study of streaming potential measurements in the case of developing flow at Reynolds numbers up to and beyond transition to turbulence and found that the flow field must be fully developed over at least 90% of the channel length in order to achieve accurate streaming potential measurements.[50] Finally, the streaming potential method also suffers from the challenge of measuring sometimes highly sensitive voltage differences. For example, the original form of the ZetaSpin technique (an adaptation of the streaming potential method described in more detail below) was limited to solutions with electrolyte concentrations less than 1 mM.[51] Above this concentration, streaming potentials were less than 0.1 mV and became difficult to distinguish from noise.

Streaming current method

The streaming current method is closely related to the streaming potential method, except that the equilibrium streaming current is measured as a function of the applied driving pressure difference instead of the streaming potential. That is, with streaming potential measurements, a high-impedance voltmeter is applied across the channel, whereas with streaming current measurements, a low-impedance ammeter is used. A modified form of the Helmholtz-Smoluchowski equation can then be used to deduce the zeta potential from the streaming current versus pressure drop relationship. As a standalone measurement technique, the streaming current method has had less popularity than the streaming potential method, although hybrid methods using both streaming potential and streaming current measurements have been developed to provide more accurate results and to simultaneously measure additional properties such as the surface conductivity.[52,53] For example, subsequent studies of the ZetaSpin technique (described below) demonstrated the use of streaming current measurements in conjunction with streaming potential measurements to experimentally determine a current collection efficiency for a system that is insensitive to the zeta potential and solute concentration, which allows the system to be used to measure zeta potentials at much higher solution conductivities than with streaming potential measurements alone.[54] In addition, Werner *et al.* developed a Microslit Electrokinetic Set-up (MES) and demonstrated the simultaneous measurement of the zeta potential and surface conductivity of planar surface samples through a combination of streaming potential and streaming current measurements.[53] Due to its close similarity to the streaming potential method, the streaming current method suffers from many of the challenges as described in the previous section.

ZetaSpin method

A more recent technique that solves some of the challenges of traditional streaming potential/current approaches is the ZetaSpin method. Sides and Hoggard developed the first iteration of the ZetaSpin technique, which consists of a disk-shaped test surface that is spun in the plane normal to its axis in contact with an electrolyte solute solution.[51] The authors showed that voltage measurements, one near the surface on the axis of rotation and one far from the disk, can be used to directly predict the zeta potential of the surface, and that the measured streaming potential varies with the rotation rate to the $\frac{3}{2}$ power.[51] This ZetaSpin technique eliminated the need to carefully seal flow channels in order to withstand the pressures of traditional streaming potential/current methods, and it also eliminated the need for corrections due to the presence of another material. The most limiting constraint for this approach is the limitation to electrolyte concentrations less than 1 mM. Sides and Hoggard found that above this level the streaming potentials were much less than 1 mV and could not be measured reliably.[51]

Hoggard *et al.* improved on the ZetaSpin technique and extended the technique to measure ζ at higher solute concentrations by incorporating streaming current measurements into the system.[54] By varying the geometry of the outer electrode, they measured the current collection efficiencies for each variant and found that they are insensitive to both the zeta potential and electrolyte concentration in solution.[54] Once the current collection efficiency is known for a given system, the true streaming current can be estimated from the measured current, and the zeta potential can then be predicted. A revised theory for the ZetaSpin method was later introduced that better accounted for the radially outward flow of mobile charge near the surface and improved the accuracy of ζ predictions.[55] This technique has been used successfully to measure the zeta potentials of many general-use materials including paints, plastics, minerals, and glass.[56] Another significant advantage for the ZetaSpin technique is that the surface conductivity is negligible for all practical electrolyte concentrations, which means that correction factors are not needed as in traditional streaming potential/current methods.[57]

While the ZetaSpin technique has demonstrated success and reliability, some features of this technique may present limitations for certain types of measurements. The technique is sensitive to the position of the near-surface electrode, especially to its distance from the surface. With the basic streaming potential approach, measurements are limited to less than 1 mM electrolyte concentrations. With the hybrid streaming potential/current method, this limitation is eliminated, but current collection efficiencies are typically small, on the order of 1-3%, and the measured currents are on the order of 10 nA. This approach also requires calibration experiments depending on the chosen outer electrodes, since collection efficiencies are sensitive to the size and shape of the electrodes. Finally, it is unclear whether electrode polarization introduces a source of uncertainty in this system since the flow cannot be reversed to detect asymmetric measurements as in the traditional streaming potential approach. Nonetheless, the ZetaSpin technique remains an attractive, general-purpose method for measuring the zeta potentials of surfaces exposed to electrolyte solutions.

Appendix B: Numerical Simulations

As mentioned, numerical simulations were performed using the OpenFOAM[35] computational fluid dynamics toolbox. A custom, in-house solver based on the simpleFoam and scalarTransportFoam solvers of OpenFOAM was designed to simultaneously solve for the coupled steady-state fluid/solute dynamics under the influence of diffusioosmosis. The solver operates by iteratively solving for the quasi-steady fluid velocity and pressure using the simpleFoam solver and then updating the solute concentration profile using the transient scalarTransportFoam solver. This separation of time scales is made possible by the low Reynolds number flow assumption and by the large separation in the time scales of viscous and solute diffusion (i.e. $\nu \gg D_s$). The solver is run until the solute concentration profile no longer evolves with time, at which point both the solute and fluid dynamics have reached their steady-state profiles. The solver is second-order accurate in space. Each simulation used approximately 3×10^5 grid cells and converged in about 5 minutes running on 64 processors.

Simulation meshes were designed using OpenFOAM's built-in blockMesh and refineMesh utilities with local refinements near the inlet and outlet of the pore to efficiently resolve the junctions with the main channel flows. A subset of the simulation domain demonstrates this strategy of local refinement at the junctions in Figure 8. The axial distribution of grid cells within the pore are refined towards the outlet, so that the finest mesh occurs in the vicinity of the pore's outlet, which is the most critical region to resolve since diffusioosmosis is strongest there. For this reason, the dynamics near the pore inlet are relatively unimportant. In fact, performing simulations without the side channel adjacent to the pore inlet (channel 1 in Figure 1) and simply fixing the inlet conditions at the pore entrance results in identical numerical results when compared with simulations of the full system with both side channels. Furthermore, with this strategy the average flow speed in the pore $\bar{U}$ can be set directly as an input parameter to the simulation, whereas with both side channels included, $\bar{U}_{\mathrm{main},1}$ and $\bar{U}_{\mathrm{main},2}$ are set as input parameters, and $\bar{U}$ must be measured. Therefore, most simulations were performed without the side channel 1 (which we confirmed had a negligible impact on results) in order to more conveniently perform simulations over a range of desired $\Gamma_w / L\bar{U}$ and Pe values.

At solid boundaries, the no-penetration boundary condition was enforced for the velocity component normal to the walls, and the diffusioosmotic wall slip velocity boundary condition given by Eq. (3) was enforced for the velocity components tangent to the wall. The pressure gradient normal to the walls was fixed to be zero. At the outlet(s) of the system, the velocity was given a zero normal gradient boundary condition, which assumes the flow is fully developed and the pressure was fixed at a uniform value of zero. Finally, at the inlet(s) the pressure was given a zero normal gradient boundary condition, and $\bar{U}_{\mathrm{main},1}$ and $\bar{U}_{\mathrm{main},2}$ (or $\bar{U}$ and $\bar{U}_{\mathrm{main},2}$ depending on whether channel 1 was included in the simulation) were fixed at uniform values.

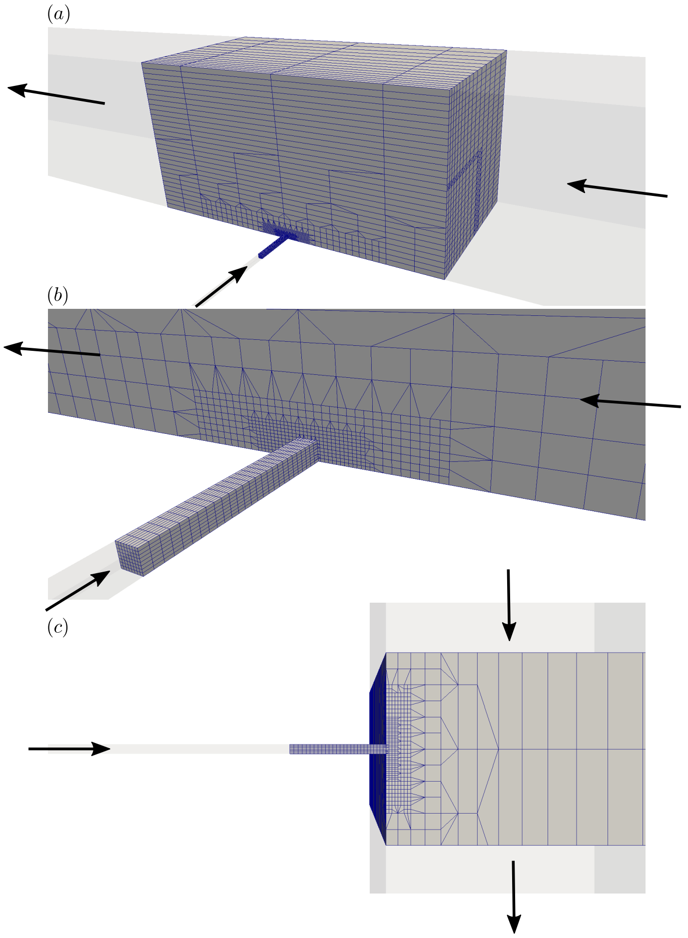

Fig. 8 Sample subset of the numerical simulation domain showing the local refinement strategy used to merge the outlet of the pore with the relatively much larger main channel. Only grid cells in the vicinity of the junction are visualized to demonstrate these local refinements. Mesh visualizations include (a) perspective view of the junction, (b) close-up perspective view of the junction, and (c) bottom-up view of the junction. As can be seen, five levels of progressive refinement were used to match the pore to the side main channel. Solid arrows denote the direction of the flow. Mesh resolutions shown have been coarsened purposefully by a factor of two in all directions for visualization purposes.

References

1 C. Lee, C. Cottin-Bizonne, A.-L. Biance, P. Joseph, L. Bocquet and C. Ybert, *Phys. Rev. Lett.*, 2014, **112**, 244501.

2 B. J. Kirby, *Micro- and Nanoscale Fluid Mechanics: Transport in Microfluidic Devices*, Cambridge university press, 2010.

3 A. T. Conlisk, *Essentials of Micro-and Nanofluidics: with Applications to the Biological and Chemical Sciences*, Cambridge University Press, 2012.

4 J. L. Anderson, *Ann. Rev. Fluid Mech.*, 1989, **21**, 61–99.

5 D. Velegol, A. Garg, R. Guha, A. Kar and M. Kumar, *Soft Matter*, 2016, **12**, 4686–4703.

6 J. Palacci, B. Abécassis, C. Cottin-Bizonne, C. Ybert and L. Bocquet, *Phys. Rev. Lett.*, 2010, **104**, 138302.

7 S. Shin, J. T. Ault, P. B. Warren and H. A. Stone, *Phys. Rev. X*, 2017, **7**, 041038.

8 S. M. Friedrich, J. M. Burke, K. J. Liu, C. F. Ivory and T.-H. Wang, *Nature Commun.*, 2017, **8**, 1213.

9 D. Florea, S. Musa, J. M. R. Huyghe and H. M. Wyss, *Proc. Natl. Acad. Sci. U.S.A.*, 2014, **111**, 6554–6559.

10 S. Shin, O. Shardt, P. B. Warren and H. A. Stone, *Nat. Commun.*, 2017, **8**, 15181.

11 H. Lee, J. Kim, J. Yang, S. W. Seo and S. J. Kim, *Lab Chip*, 2018, **18**, 1713–1724.

12 A. Kar, T.-Y. Chiang, I. O. Rivera, A. Sen and D. Velegol, *ACS Nano*, 2015, **9**, 746–753.

13 S. Shin, E. Um, B. Sabass, J. T. Ault, M. Rahimi, P. B. Warren and H. A. Stone, *Proc. Natl. Acad. Sci. U.S.A.*, 2016, **113**, 257–261.

14 J. T. Ault, P. B. Warren, S. Shin and H. A. Stone, *Soft Matter*, 2017, **13**, 9015–9023.

15 R. P. Sear and P. B. Warren, *Phys. Rev. E*, 2017, **96**, 062602.

16 F. Boulogne, S. Shin, J. Dervaux, L. Limat and H. A. Stone, *Soft Matter*, 2017, **13**, 5122–5129.

17 R. Guha, F. Mohajerani, A. Mukhopadhyay, M. D. Collins, A. Sen and D. Velegol, *ACS Appl. Mater. Interfaces*, 2017, **9**, 43352–43362.

18 S. Shin, J. T. Ault, J. Feng, P. B. Warren and H. A. Stone, *Adv. Mater.*, 2017, **29**, 1701516.

19 S. Shin, P. B. Warren and H. A. Stone, *Phys. Rev. Appl.*, 2018, **9**, 034012.

20 J. L. Anderson, M. E. Lowell and D. C. Prieve, *J. Fluid Mech.*, 1982, **117**, 107–121.

21 J. L. Anderson and D. C. Prieve, *Separ. Purif. Method*, 1984, **13**, 67–103.

22 P. O. Staffeld and J. A. Quinn, *J. Colloid Interf. Sci.*, 1989, **130**, 88–100.

23 B. Ball and D. W. Fuerstenau, *Miner. Sci. Eng*, 1973, **5**, 267–277.

24 H. Ohshima and T. Kondo, *J. Colloid Interf. Sci.*, 1990, **135**, 443–448.

25 A. Szymczyk, P. Fievet, M. Mullet, J. C. Reggiani and J. Pagetti, *J. Membrane Sci.*, 1998, **143**, 189–195.

26 P. R. Johnson, *J. Colloid Interf. Sci.*, 1999, **209**, 264–267.

27 B. V. Derjaguin, S. S. Dukhin and A. A. Korotkova, *Kolloid. Zh.*, 1961, **23**, 53–58.

28 B. V. Derjaguin, G. P. Sidorenkov, E. A. Zubashchenko and E. V. Kiseleva, *Kolloid. Zh.*, 1947, **9**, 335–348.

29 B. V. Derjaguin, S. S. Dukhin and M. M. Koptelova, *J. Colloid Interf. Sci.*, 1972, **38**, 584–595.

30 J. L. Anderson and D. M. Malone, *Biophys. J.*, 1974, **14**, 957–982.

31 J. L. Anderson, *J. Theor. Biol.*, 1981, **90**, 405–426.

32 J. T. Ault, S. Shin and H. A. Stone, *J. Fluid Mech.*, 2018, **854**, 420–448.

33 F. M. White and I. Corfield, *Viscous Fluid Flow*, McGraw-Hill New York, 2006, vol. 3.

34 B. J. Kirby and E. F. Hasselbrink Jr., *Electrophoresis*, 2004, **25**, 187–202.

35 H. H. Weller, G. Tabor, H. Jasak and C. Fureby, *Comput. Phys.*, 1998, **12**, 620–631.

36 M. von Smoluchowski, *Bull. Akad. Sci. Cracovie.*, 1903, **8**, 182–200.

37 A. Sze, D. Erickson, L. Ren and D. Li, *J. Colloid Interf. Sci.*, 2003, **261**, 402–410.

38 B. J. Kirby and E. F. Hasselbrink Jr., *Electrophoresis*, 2004, **25**, 203–213.

39 D. J. Shaw, *Electrophoresis*, Academic Press, 1969.

40 M. Elimelech, W. H. Chen and J. J. Waypa, *Desalination*, 1994, **95**, 269–286.

41 D. Yan, N.-T. Nguyen, C. Yang and X. Huang, *J. Chem. Phys.*, 2006, **124**, 021103.

42 J. C. W. Corbett, F. McNeil-Watson, R. O. Jack and M. Howarth, *Colloid Surface A*, 2012, **396**, 169–176.

43 A. Vernhet, C. Bellon-Fontaine and A. Doren, *J. Chim. Phys.*, 1994, **91**, 1728–1747.

44 H.-J. Jacobasch, G. Bauböck and J. Schurz, *Colloid Polym. Sci.*, 1985, **263**, 3–24.

45 H.-J. Jacobasch and J. Schurz, in *Dispersed systems*, Springer, 1988, pp. 40–48.

46 P. J. Scales, F. Grieser, T. W. Healy, L. R. White and D. Y. C. Chan, *Langmuir*, 1992, **8**, 965–974.

47 A. E. Childress and M. Elimelech, *J. Membrane Sci.*, 1996, **119**, 253–268.

48 A. E. Childress and M. Elimelech, *Environ. Sci. Technol.*, 2000, **34**, 3710–3716.

49 A. E. Childress and S. S. Deshmukh, *Desalination*, 1998, **118**, 167–174.

50 R. A. Van Wagenen and J. D. Andrade, *J. Colloid Interf. Sci.*, 1980, **76**, 305–314.

51 P. J. Sides and J. D. Hoggard, *Langmuir*, 2004, **20**, 11493–11498.

52 H. Xie, T. Saito and M. A. Hickner, *Langmuir*, 2011, **27**, 4721–4727.

53 C. Werner, R. Zimmermann and T. Kratzmüller, *Colloid Surface A*, 2001, **192**, 205–213.

54 J. D. Hoggard, P. J. Sides and D. C. Prieve, *Langmuir*, 2005, **21**, 7433–7438.

55 P. J. Sides, J. Newman, J. D. Hoggard and D. C. Prieve, *Langmuir*, 2006, **22**, 9765–9769.

56 F. S. Lameiras, A. L. d. Souza, V. A. R. d. Melo, E. H. M. Nunes and I. D. Braga, *Mater. Res.*, 2008, **11**, 217–219.

57 P. J. Sides and D. C. Prieve, *Langmuir*, 2013, **29**, 13427–13432.